Energy dependence of polarized $\gamma\gamma \to e^+e^-$ in peripheral Au + Au collisions at $\sqrt{s_{NN}} = 54.4$ and 200 GeV with the STAR experiment at RHIC

M. I. Abdulhamid,[5] B. E. Aboona,[58] J. Adam,[17] J. R. Adams,[43] G. Agakishiev,[32] I. Aggarwal,[44] M. M. Aggarwal,[44] Z. Ahammed,[64] A. Aitbaev,[32] I. Alekseev,[3,40] E. Alpatov,[40] A. Aparin,[32] S. Aslam,[28] J. Atchison,[2] G. S. Averichev,[32] V. Bairathi,[56] J. G. Ball Cap,[24] K. Barish,[12] P. Bhagat,[31] A. Bhasin,[31] S. Bhatta,[55] I. G. Bordyuzhin,[3] J. D. Brandenburg,[43] A. V. Brandin,[40] C. Broodo,[24] X. Z. Cai,[53] H. Caines,[67] M. Calderón de la Barca Sánchez,[10] D. Cebra,[10] J. Ceska,[17] I. Chakaberia,[36] B. K. Chan,[11] Z. Chang,[29] A. Chatterjee,[18] D. Chen,[12] J. Chen,[52] J. H. Chen,[21] Q. Chen,[22] Z. Chen,[52] J. Cheng,[60] Y. Cheng,[11] W. Christie,[7] X. Chu,[7] H. J. Crawford,[9] G. Dale-Gau,[14] A. Das,[17] T. G. Dedovich,[32] I. M. Deppner,[23] A. A. Derevschikov,[45] A. Deshpande,[55] A. Dhamija,[44] P. Dixit,[26] X. Dong,[36] J. L. Drachenberg,[2] E. Duckworth,[33] J. C. Dunlop,[7] J. Engelage,[9] G. Eppley,[47] S. Esumi,[61] O. Evdokimov,[14] O. Eyser,[7] R. Fatemi,[34] S. Fazio,[8] C. J. Feng,[42] Y. Feng,[46] E. Finch,[54] Y. Fisyak,[7] F. A. Flor,[67] C. Fu,[30] T. Gao,[52] F. Geurts,[47] N. Ghimire,[57] A. Gibson,[63] K. Gopal,[27] X. Gou,[52] D. Grosnick,[63] A. Gupta,[31] A. Hamed,[5] Y. Han,[47] M. D. Harasty,[10] J. W. Harris,[67] H. Harrison-Smith,[34] L. B. Havener,[67] W. He,[21] X. H. He,[30] Y. He,[52] C. Hu,[62] Q. Hu,[30] Y. Hu,[36] H. Huang,[42] H. Z. Huang,[11] S. L. Huang,[55] T. Huang,[14] Y. Huang,[60] Y. Huang,[13] T. J. Humanic,[43] M. Isshiki,[61] W. W. Jacobs,[29] A. Jalotra,[31] C. Jena,[27] Y. Ji,[36] J. Jia,[55,7] C. Jin,[47] X. Ju,[49] E. G. Judd,[9] S. Kabana,[56] D. Kalinkin,[34] K. Kang,[60] D. Kapukchyan,[12] K. Kauder,[7] D. Keane,[33] A. Kechechyan,[32] A. Khanal,[65] A. Kiselev,[7] A. G. Knospe,[37] H. S. Ko,[36] L. Kochenda,[40] A. A. Korobitsin,[32] A. Yu. Kraeva,[40] P. Kravtsov,[40] L. Kumar,[44] M. C. Labonte,[10] R. Lacey,[55] J. M. Landgraf,[7] A. Lebedev,[7] R. Lednicky,[32] J. H. Lee,[7] Y. H. Leung,[23] C. Li,[13] D. Li,[49] H.-S. Li,[46] H. Li,[66] H. Li,[22] W. Li,[47] X. Li,[49] Y. Li,[49] Y. Li,[60] Z. Li,[49] X. Liang,[12] Y. Liang,[33] T. Lin,[52] Y. Lin,[22] C. Liu,[30] G. Liu,[50] H. Liu,[13] L. Liu,[13] T. Liu,[67] X. Liu,[43] Y. Liu,[58] Z. Liu,[13] T. Ljubicic,[47] O. Lomicky,[17] R. S. Longacre,[7] E. M. Loyd,[12] T. Lu,[30] J. Luo,[49] X. F. Luo,[13] V. B. Luong,[32] L. Ma,[21] R. Ma,[7] Y. G. Ma,[21] N. Magdy,[55] R. Manikandhan,[24] O. Matonoha,[17] G. McNamara,[65] O. Mezhanska,[17] K. Mi,[13] N. G. Minaev,[45] B. Mohanty,[41] B. Mondal,[41] M. M. Mondal,[41] I. Mooney,[67] D. A. Morozov,[45] M. I. Nagy,[19] C. J. Naim,[55] A. S. Nain,[44] J. D. Nam,[57] M. Nasim,[26] E. Nedorezov,[32] D. Neff,[11] J. M. Nelson,[9] M. Nie,[52] G. Nigmatkulov,[14] T. Niida,[61] L. V. Nogach,[45] T. Nonaka,[61] G. Odyniec,[36] A. Ogawa,[7] S. Oh,[51] V. A. Okorokov,[40] K. Okubo,[61] B. S. Page,[7] S. Pal,[17] A. Pandav,[36] A. Panday,[26] A. K. Pandey,[30] Y. Panebratsev,[32] T. Pani,[48] P. Parfenov,[40] A. Paul,[12] C. Perkins,[9] B. R. Pokhrel,[57] I. D. Ponce Pinto,[67] M. Posik,[57] A. Povarov,[40] T. L. Protzman,[37] N. K. Pruthi,[44] J. Putschke,[65] Z. Qin,[60] H. Qiu,[30] C. Racz,[12] S. K. Radhakrishnan,[33] A. Rana,[44] R. L. Ray,[59] C. W. Robertson,[46] O. V. Rogachevsky,[32] M. A. Rosales Aguilar,[34] D. Roy,[48] L. Ruan,[7] A. K. Sahoo,[26] N. R. Sahoo,[27] H. Sako,[61] S. Salur,[48] E. Samigullin,[3] S. Sato,[61] B. C. Schaefer,[37] W. B. Schmidke,[7,*] N. Schmitz,[38] J. Seger,[16] R. Seto,[12] P. Seyboth,[38] N. Shah,[28] E. Shahaliev,[32] P. V. Shanmuganathan,[7] T. Shao,[21] M. Sharma,[31] N. Sharma,[26] R. Sharma,[27] S. R. Sharma,[27] A. I. Sheikh,[33] D. Shen,[52] D. Y. Shen,[21] K. Shen,[49] S. S. Shi,[13] Y. Shi,[52] Q. Y. Shou,[21] F. Si,[49] J. Singh,[56] S. Singha,[30] P. Sinha,[27] M. J. Skoby,[6,46] Y. Söhngen,[23] Y. Song,[67] B. Srivastava,[46] T. D. S. Stanislaus,[63] D. J. Stewart,[65] M. Strikhanov,[40] Y. Su,[49] C. Sun,[55] X. Sun,[30] Y. Sun,[49] Y. Sun,[25] B. Surrow,[57] D. N. Svirida,[3] Z. W. Sweger,[10] A. C. Tamis,[67] A. H. Tang,[7] Z. Tang,[49] A. Taranenko,[40] T. Tarnowsky,[39] J. H. Thomas,[36] D. Tlusty,[16] T. Todoroki,[61] M. V. Tokarev,[32] S. Trentalange,[11] P. Tribedy,[7] O. D. Tsai,[11,7] C. Y. Tsang,[33,7] Z. Tu,[7] J. Tyler,[58] T. Ullrich,[7] D. G. Underwood,[4,63] I. Upsal,[49] G. Van Buren,[7] A. N. Vasiliev,[45,40] V. Verkest,[65] F. Videbæk,[7] S. Vokal,[32] S. A. Voloshin,[65] G. Wang,[11] J. S. Wang,[25] J. Wang,[52] K. Wang,[49] X. Wang,[52] Y. Wang,[49] Y. Wang,[13] Y. Wang,[60] Z. Wang,[52] J. C. Webb,[7] P. C. Weidenkaff,[23] G. D. Westfall,[39] H. Wieman,[36] G. Wilks,[14] S. W. Wissink,[29] J. Wu,[13] J. Wu,[30] X. Wu,[11] X. Wu,[49] B. Xi,[21] Z. G. Xiao,[60] G. Xie,[62] W. Xie,[46] H. Xu,[25] N. Xu,[36] Q. H. Xu,[52] Y. Xu,[52] Y. Xu,[13] Z. Xu,[33] Z. Xu,[11] G. Yan,[52] Z. Yan,[55] C. Yang,[52] Q. Yang,[52] S. Yang,[50] Y. Yang,[1,42] Z. Ye,[50] Z. Ye,[36] L. Yi,[52] Y. Yu,[52] W. Zha,[49] C. Zhang,[21] D. Zhang,[50] J. Zhang,[52] S. Zhang,[15] W. Zhang,[50] X. Zhang,[30] Y. Zhang,[30] Y. Zhang,[49] Y. Zhang,[52] Y. Zhang,[22] Z. J. Zhang,[42] Z. Zhang,[7] Z. Zhang,[14] F. Zhao,[35] J. Zhao,[21] M. Zhao,[7] S. Zhou,[13] Y. Zhou,[13] X. Zhu,[60] M. Zurek,[4,7] and M. Zyzak[20]

(STAR Collaboration)

[1]*Academia Sinica, Taipei*

[2]*Abilene Christian University, Abilene, Texas 79699*

[3]*Alikhanov Institute for Theoretical and Experimental Physics NRC "Kurchatov Institut", Moscow 117218*

[4]*Argonne National Laboratory, Argonne, Illinois 60439*

[5]*American University in Cairo, New Cairo 11835, Egypt*

[6]*Ball State University, Muncie, Indiana, 47306*

[7]*Brookhaven National Laboratory, Upton, New York 11973*

[8]*University of Calabria & INFN-Cosenza, Rende 87036, Italy*

[9]*University of California, Berkeley, California 94720*

[10]*University of California, Davis, California 95616*

[*]Deceased.

[11]*University of California, Los Angeles, California 90095*
[12]*University of California, Riverside, California 92521*
[13]*Central China Normal University, Wuhan, Hubei 430079*
[14]*University of Illinois at Chicago, Chicago, Illinois 60607*
[15]*Chongqing University, Chongqing 401331*
[16]*Creighton University, Omaha, Nebraska 68178*
[17]*Czech Technical University in Prague, FNSPE, Prague 115 19, Czech Republic*
[18]*National Institute of Technology Durgapur, Durgapur 713209, India*
[19]*ELTE Eötvös Loránd University, Budapest H-1117, Hungary*
[20]*Frankfurt Institute for Advanced Studies FIAS, Frankfurt 60438, Germany*
[21]*Fudan University, Shanghai 200433*
[22]*Guangxi Normal University, Guilin 541004*
[23]*University of Heidelberg, Heidelberg 69120, Germany*
[24]*University of Houston, Houston, Texas 77204*
[25]*Huzhou University, Huzhou, Zhejiang 313000*
[26]*Indian Institute of Science Education and Research (IISER), Berhampur 760010, India*
[27]*Indian Institute of Science Education and Research (IISER) Tirupati, Tirupati 517507, India*
[28]*Indian Institute Technology, Patna, Bihar 801106, India*
[29]*Indiana University, Bloomington, Indiana 47408*
[30]*Institute of Modern Physics, Chinese Academy of Sciences, Lanzhou, Gansu 730000*
[31]*University of Jammu, Jammu 180001, India*
[32]*Joint Institute for Nuclear Research, Dubna 141 980*
[33]*Kent State University, Kent, Ohio 44242*
[34]*University of Kentucky, Lexington, Kentucky 40506-0055*
[35]*Lanzhou University, Lanzhou*
[36]*Lawrence Berkeley National Laboratory, Berkeley, California 94720*
[37]*Lehigh University, Bethlehem, Pennsylvania 18015*
[38]*Max-Planck-Institut für Physik, Munich 80805, Germany*
[39]*Michigan State University, East Lansing, Michigan 48824*
[40]*National Research Nuclear University MEPhI, Moscow 115409*
[41]*National Institute of Science Education and Research, HBNI, Jatni 752050, India*
[42]*National Cheng Kung University, Tainan 70101*
[43]*The Ohio State University, Columbus, Ohio 43210*
[44]*Panjab University, Chandigarh 160014, India*
[45]*NRC "Kurchatov Institut", Institute of High Energy Physics, Protvino 142281*
[46]*Purdue University, West Lafayette, Indiana 47907*
[47]*Rice University, Houston, Texas 77251*
[48]*Rutgers University, Piscataway, New Jersey 08854*
[49]*University of Science and Technology of China, Hefei, Anhui 230026*
[50]*South China Normal University, Guangzhou, Guangdong 510631*
[51]*Sejong University, Seoul, 05006, South Korea*
[52]*Shandong University, Qingdao, Shandong 266237*
[53]*Shanghai Institute of Applied Physics, Chinese Academy of Sciences, Shanghai 201800*
[54]*Southern Connecticut State University, New Haven, Connecticut 06515*
[55]*State University of New York, Stony Brook, New York 11794*
[56]*Instituto de Alta Investigación, Universidad de Tarapacá, Arica 1000000, Chile*
[57]*Temple University, Philadelphia, Pennsylvania 19122*
[58]*Texas A&M University, College Station, Texas 77843*
[59]*University of Texas, Austin, Texas 78712*
[60]*Tsinghua University, Beijing 100084*
[61]*University of Tsukuba, Tsukuba, Ibaraki 305-8571, Japan*
[62]*University of Chinese Academy of Sciences, Beijing, 101408*
[63]*Valparaiso University, Valparaiso, Indiana 46383*
[64]*Variable Energy Cyclotron Centre, Kolkata 700064, India*
[65]*Wayne State University, Detroit, Michigan 48201*
[66]*Wuhan University of Science and Technology, Wuhan, Hubei 430065*
[67]*Yale University, New Haven, Connecticut 06520*

(Received 23 July 2024; revised 13 October 2024; accepted 9 December 2024; published 16 January 2025)

We report the differential yields at mid-rapidity of the Breit-Wheeler process ($\gamma\gamma \to e^+e^-$) in peripheral Au + Au collisions at $\sqrt{s_{NN}} = 54.4$ and 200 GeV with the STAR experiment at the Relativistic Heavy Ion Collider (RHIC), as a function of energy $\sqrt{s_{NN}}$, e^+e^- transverse momentum p_{T}, p_{T}^2, invariant mass M_{ee}, and azimuthal angle. In the invariant mass range of $0.4 < M_{ee} < 2.6$ GeV/c^2 at low transverse momentum ($p_{\mathrm{T}} < 0.15$ GeV/c), the yields increase while the pair $\sqrt{\langle p_{\mathrm{T}}^2 \rangle}$ decreases with increasing $\sqrt{s_{NN}}$, a feature that is correctly predicted by the QED calculation. The energy dependencies of the measured quantities are sensitive to the nuclear form factor, infrared divergence and photon polarization. The data are compiled and used to extract the charge radius of the Au nucleus.

DOI: 10.1103/PhysRevC.111.014909

I. INTRODUCTION

In ultrarelativistic heavy-ion collisions, strong electromagnetic fields arising from the Lorentz contraction of highly charged nuclei generate a large flux of high-energy quasireal photons (equivalent photon approximation, EPA) [1,2]. In collisions of identical nuclei, the photon density is proportional to the square of the ion charge number (Z). Dileptons can be produced via photon-photon interactions ($\gamma\gamma \to l^+l^-$) even in ultraperipheral heavy-ion collisions (UPCs) for which the impact parameter between the colliding nuclei is larger than the sum of their radii such that no nuclear overlap occurs [3–6]. From the EPA, the photons are preferentially aligned along the collision axis and have transverse momentum on the scale of ω/γ_L, where ω is the photon energy and γ_L is the Lorentz factor of the colliding nuclei. Therefore, the leptons produced by these photon-photon processes have the distinctive signature of being nearly back to back in azimuth with small pair transverse momenta [7]. Traditionally these photon-photon fusion processes have been studied only in UPCs [8–13]. However, it was recently observed that even in hadronic heavy-ion collisions (HHICs) the dilepton production at very low transverse momentum (p_{T}) originates mainly from two-photon interactions [14–16]. Furthermore, the STAR Collaboration at the Relativistic Heavy-ion Collider (RHIC) [14] and the ATLAS Collaboration at the Large Hadron Collider (LHC) [15] have found a significant pair p_{T} broadening effect for the lepton pairs from photon-photon collisions in HHICs compared to those in UPCs. Previously, it was believed that the transverse momentum distribution of dileptons from the two-photon process should not depend on the impact parameter, and the observed broadening of p_{T} was explained by introducing the final-state effect of either the Lorentz force from a trapped electromagnetic field [14] or Coulomb scattering [15] in the quark-gluon plasma (QGP) created in the HHICs. In contrast to these expectations, recent measurements in Pb + Pb UPCs by the CMS Collaboration, where the final-state effects are absent, show that the dimuons produced via two-photon process have significant impact parameter dependence [17]. CMS also measured the p_{T} broadening effect, which has quantitatively been described by the generalized EPA (gEPA), lowest order QED, and Wigner function formalism, each of which includes the impact parameter dependence [7,18–21]. The broadening effect due to the initial QED field strength should be considered in studying possible trapped magnetic field and multiple scattering in QGP. Specifically, QED calculations with the impact parameter dependence of initial photon kinematics predict a systematically lower $\sqrt{\langle p_{\mathrm{T}}^2 \rangle}$ than the STAR data [7] in HHICs. More experimental studies in the peripheral HHICs are crucial for understanding such a discrepancy and to investigate the potential final-state effects.

According to the EPA [8,11], the photon number density as a function of energy ω is determined by the field of a single nucleus:

$$n(\omega) = \frac{(Ze)^2}{\pi\omega} \int_0^\infty \frac{d^2k_\perp}{(2\pi)^2} \left[\frac{F\left(\left(\frac{\omega}{\gamma_L}\right)^2 + \vec{k}_\perp^{\,2}\right)}{\left(\frac{\omega}{\gamma_L}\right)^2 + \vec{k}_\perp^{\,2}} \right]^2 \vec{k}_\perp^{\,2}, \quad (1)$$

where $\vec{k}_\perp$ is the photon transverse momentum, and $F((\frac{\omega}{\gamma_L})^2 + \vec{k}_\perp^{\,2})$ is the nuclear electromagnetic form factor. The photon-photon process is categorized into three possible interactions according to the virtuality of the photons [19]: the collision of two virtual photons (Landau-Lifschitz process [22]); the collision of one virtual and one real photon (Bethe-Heitler process [23]); and the collision of two real photons (Breit-Wheeler process [24]). The transverse momentum of the photons in UPCs is often considered to be related to the virtuality of the photons [5,9,25–27]. Therefore, the two-photon process in UPCs is considered to be the Landau-Lifschitz process. However, in many practical calculations, the Breit-Wheeler formalism is applied as a convenient and practical tool [28] ignoring any possible effect from small virtuality. There is no clear consensus on what is considered as the Breit-Wheeler process in UPCs. Constraints on the available phase space for the photons that may participate in the Breit-Wheeler process in heavy-ion collisions were recently proposed [29]:

$$\omega/\gamma_L \lesssim k_\perp \lesssim 1/R \ll \omega, \quad (2)$$

where R is the charge radius of the colliding nucleus. Due to the STAR kinematic acceptance requirement of single electron (positron) transverse momentum being greater than 200 MeV/c at midrapidity (with pseudorapidity $|\eta| < 1$), there may not be sufficient phase space for the Breit-Wheeler process as defined in relation (2) at low beam energies ($\gamma_L \lesssim 20$) even though the Breit-Wheeler process dominates at top RHIC energy. Distinctive features of the Breit-Wheeler process have been found in recent STAR measurements for Au + Au collisions at 200 GeV [19]. Because real photons with zero mass cannot exist in a helicity $J_Z = 0$ state, the produced e^+e^- pair in a collision of two real photons should have a smooth invariant mass (M_{ee}) spectrum and single electron (positron)

momentum preferentially aligned along the collision axis. STAR also confirmed with a pure fourth-order azimuthal angular modulation that the quasi-real photons originating from EPA of Lorentz contraction of electromagnetic fields are linearly polarized [19]. Furthermore, Eq. (1) shows an intriguing factor $[(\frac{\omega}{\gamma_L})^2 + \overrightarrow{k}_\perp^2]$ inside the form factor (F) and in the denominator. It constrains the dielectrons produced by real photon-photon processes to have small total transverse momentum. More importantly, it suggests that the total transverse momentum (related to $\overrightarrow{k}_\perp$) increases with decreasing beam energy (γ_L) for a given photon energy (ω) [29].

In this paper, we report the energy and centrality dependence of the polarized $\gamma\gamma \to e^+e^-$ process in peripheral Au + Au collisions at $\sqrt{s_{NN}} = 54.4$ and 200 GeV. The e^+e^- yields are presented as a function of pair transverse momentum p_{T}, M_{ee}, p_{T}^2, and $\Delta\phi$, the difference between the azimuthal angles of the sum and difference of the e^+ and e^- momenta. The measurement of p_{T}^2 can better reflect whether p_{T} has a broadening effect. The yields and $\sqrt{\langle p_{\mathrm{T}}^2\rangle}$ are also presented as functions of collision energy. Furthermore, we present the measurement of $\langle\cos(4\Delta\phi)\rangle$ as a function of p_{T} predicted for the Breit-Wheeler photon-photon fusion process. Model calculations are compared with the measurements. The paper is organized as follows. Section II describes the experimental setup and the data sets used in this analysis. Section III explains in detail the analysis techniques, including event and track selection, centrality definition, electron identification, raw signal reconstruction, background subtraction, detector efficiency correction, hadronic cocktail simulation, and systematic uncertainties. Section IV presents our results on photon-induced dielectron production yields within the STAR detector acceptance and a comparison to theoretical calculations. Our results and conclusions are summarized in Sec. V.

II. EXPERIMENTAL SETUP AND DATA SETS

This experiment was conducted at the Relativistic Heavy Ion Collider (RHIC) [30], and the data were collected by the Solenoidal Tracker at RHIC (STAR) experiment. The major detector subsystems used in this analysis are the time projection chamber (TPC) [31], the barrel time of flight (TOF) [32], and a trigger subsystem: the vertex position detectors (VPDs) [33]. The TPC is the main tracking detector, used for the measurements of charged particle momenta and for particle identification (PID) via ionization energy loss per unit length (dE/dx). The TOF system consists of the barrel TOF (BTOF) detector covering the TPC outer cylinder and the VPDs at the forward pseudorapidity regions. Combining the timing information from the VPD and the BTOF detectors, the flight time of the particle can be calculated. The flight time of the particle is further combined with the track length and momentum, both measured by the TPC, to provide charged particle identification. The datasets of Au + Au collisions taken in 2010 and 2011 at $\sqrt{s_{NN}} = 200$ GeV, and those taken in 2017 at 54.4 GeV, are used for this analysis. The minimum bias trigger is defined by requiring a coincidence between the signals from the east and west VPDs and a collision-vertex cut applied in data taking, in order to select collision events that took place near the center of the detector.

III. ANALYSIS TECHNIQUES

A. Event selection and centrality definition

Events used in this analysis were required to have a reconstructed collision vertex (primary vertex) within 30 cm of the TPC center along the beam direction to ensure uniform detector acceptance, and to be within a 2 cm radius in the plane perpendicular to the beam direction to reject events hitting the beam pipe (radius 5 cm). To suppress pileup events from different bunch crossings in which a TPC vertex was mistakenly reconstructed, the distance along the beam line between the collision vertex constructed using the TPC and that determined by the VPD is required to be less than 3 cm. These selection criteria yield 222 M (year 2010) and 508 M (year 2011) minimum bias triggered events at $\sqrt{s_{NN}} = 200$ GeV and 490 M (year 2017) minimum bias triggered events at $\sqrt{s_{NN}} = 54.4$ GeV. The results at $\sqrt{s_{NN}} = 200$ GeV reported in this paper are from the combined year 2010 and year 2011 data.

The centrality definition used in this analysis is determined by matching the TPC measured (uncorrected) charged particle multiplicity density $dN/d\eta$ within $|\eta| < 0.5$ with a Monte Carlo Glauber simulation [34,35]. The centrality bins are defined according to the Monte Carlo Glauber distribution. In particular, if the charged particle multiplicity is less than that corresponding to 80% centrality, it is defined as 80–100%.

B. Track selection

The main detector subsystems used to reconstruct the electron candidate tracks (including positrons if not specified) are the TPC and TOF. The number of fit points in the TPC (nHitsFit) is required to be at least 15–20 (this cut is different for different runs) to ensure sufficient momentum resolution, and no fewer than 10–16 (this cut is different for different runs) space points (nHitsdEdx) are required for the ionization energy loss (dE/dx) calculation to ensure good dE/dx resolution. The ratio of the number of fit points over the number of possible points should be greater than 0.52 in order to avoid track splitting in the TPC. The distance of closest approach to the primary vertex (DCA) is required to be less than 1 cm to reduce the contributions from secondary decays. Each track's transverse momentum should be greater than $0.2\,\mathrm{GeV}/c$ to ensure that the track can pass through the TPC. Furthermore, the tracks are required to match to a hit in TOF, which only covers ≈90% in azimuth.

C. Electron identification

Electrons were identified by combining the normalized dE/dx from the TPC and velocity (β) from the TOF. The normalized dE/dx is defined as follows:

$$n\sigma_e = \frac{\ln(\langle dE/dx\rangle^m/\langle dE/dx\rangle_e^{th})}{R_{dE/dx}}, \tag{3}$$

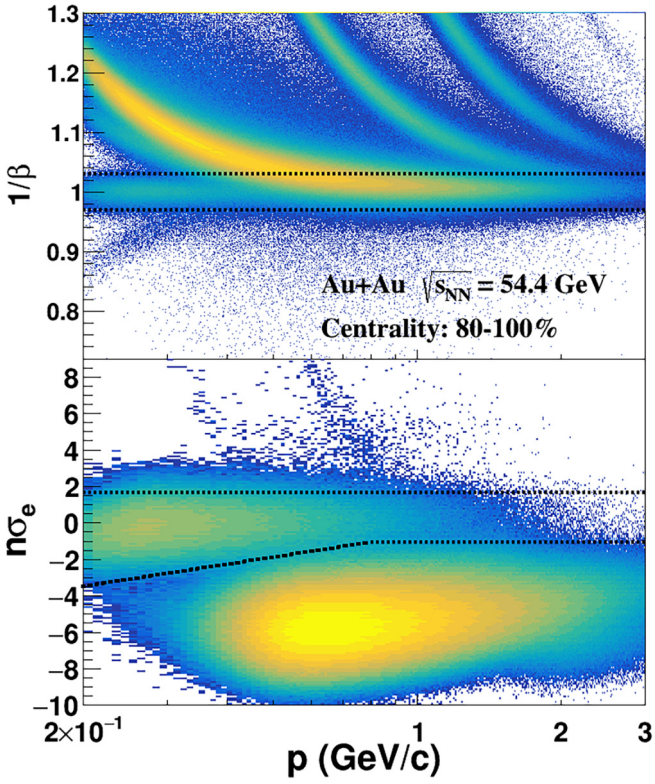

FIG. 1. An example of electron identification at $\sqrt{s_{NN}} = 54.4$ GeV in the 80–100% centrality range. Upper panel: $1/\beta$ vs momentum (p) distributions for all charged particles. Bottom panel: normalized dE/dx ($n\sigma_e$) vs p distributions after applying the TOF velocity cut $|1 - 1/\beta| < 0.03$ denoted with dashed lines.

where $\langle dE/dx\rangle^m$ and $\langle dE/dx\rangle^{th}$ represent measured and theoretical dE/dx values, respectively, and $R_{dE/dx}$ is the experimental dE/dx resolution. More details about the electron identification procedure can be found in Refs. [36,37].

The inverse particle velocity ($1/\beta$) measured by the TOF versus the particle momentum p measured by the TPC is shown in the upper panel of Fig. 1 for all charged particles in Au + Au collisions at $\sqrt{s_{NN}} = 54.4$ GeV in the 80–100% centrality range. The area enclosed by the two black lines is the TOF velocity selection condition $|1 - 1/\beta| < 0.03$. The bottom panel shows the $n\sigma_e$ vs p distribution after applying the TOF velocity selection. The area enclosed by the black lines is the selection condition from $n\sigma_e$. By making use of the measured $n\sigma_e$ and $1/\beta$, the electron sample can be selected at a high purity. The electron purity for $p_{\mathrm{T}}^e > 0.2$ GeV/c is about 95% in both the $\sqrt{s_{NN}} = 54.4$ GeV and $\sqrt{s_{NN}} = 200$ GeV data samples.

D. e^+e^- pair reconstruction and background subtraction

For each event, all electron and positron candidates within the STAR acceptance of $p_{\mathrm{T}}^e > 0.2$ GeV/c and $|\eta| < 1$ are combined to generate the (same event) inclusive unlike-sign pairs (N_{+-}, including signal and background). In this analysis the signal is defined as the e^+e^- pairs that originate from

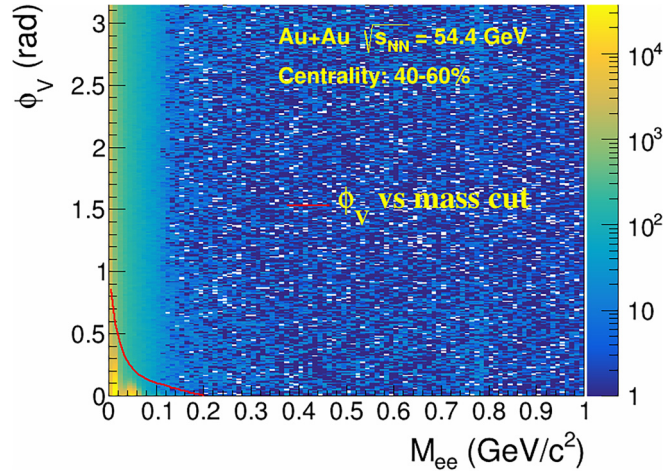

FIG. 2. ϕ_V vs mass spectrum for raw signal within the STAR acceptance in Au + Au collisions at $\sqrt{s_{NN}} = 54.4$ GeV in the centrality 40–60%. The red solid line represents the ϕ_V cut used to remove photon conversion electron pairs.

photon-photon processes. Background sources that contribute to the inclusive unlike-sign pair distributions include

(1) Combinatorial background pairs, which come from uncorrelated electron and positron pairing.
(2) Photon conversion background pairs, which come from photons interacting with the detector material and converting into e^+e^- pairs.
(3) Hadronic cocktail background pairs, which originate from hadron decays such as π^0, η, η', ω, ϕ, J/ψ, as well as correlated charmed hadrons.

Contributions from combinatorial background pairs are calculated by using the mixed-event unlike-sign pairs. The photon conversion electron pairs are removed from the same event and mixed event using the ϕ_V cut method [38,39]. This method relies on the kinematics of the pair production process. The opening angle, ϕ_V, for electron-positron pairs due to photon conversions should be zero. Unit-vector definitions used for the construction of the ϕ_V angle were taken from Refs. [37,38]. Finally, the raw dielectron signal can be obtained by subtracting the mixed-event unlike-sign pairs from the same event unlike-sign pairs. Figure 2 shows the ϕ_V vs mass spectrum for the raw signal within the STAR acceptance in Au + Au collisions at $\sqrt{s_{NN}} = 54.4$ GeV in the centrality 40–60%. In the very low invariant mass region, a clear band of photon conversion electron pairs can be observed. The red solid line represents the ϕ_V cut used to remove photon conversion electron pairs. Figure 3 shows the low-p_{T} invariant mass distributions of same event unlike-sign pairs (black dots), mixed-event unlike-sign pairs (open circles), and raw dielectron signal (blue dots) for $\sqrt{s_{NN}} = 54.4$ GeV and $\sqrt{s_{NN}} = 200$ GeV in different centralities. The significance $\frac{S}{\sqrt{S+B}}$ of the signal is also shown in Fig. 3, where S and B represent the number of raw signal and background events, respectively. Centrality 80–100% (×50) in the figure represents the experimental data for 80–100% centrality multiplied

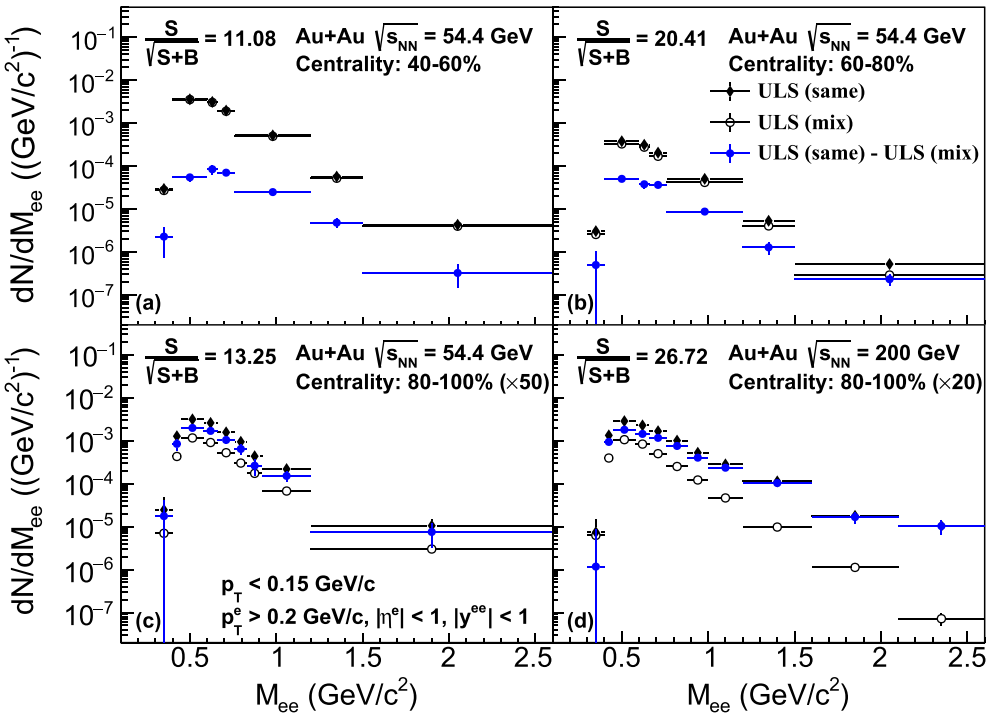

FIG. 3. The low-p_{T} ($p_{\mathrm{T}} < 0.15$ GeV/c) e^+e^- raw mass spectra within the STAR acceptance in Au + Au collisions at $\sqrt{s_{NN}} = 54.4$ GeV in the centralities (a) 40–60%, (b) 60–80%, and (c) 80–100% (scaled × 50), and (d) at $\sqrt{s_{NN}} = 200$ GeV for the 80–100% centrality range (scaled × 20). ULS (same) and ULS (mix) correspond to unlike sign in same event and mixed event, respectively. Statistical uncertainties are shown as vertical bars.

by 50, making the presentation of the figures cleaner. This approach is also applied throughout the paper.

E. Efficiency correction

The raw e^+e^- signal is corrected for the detector efficiency to obtain the final physics e^+e^- signal. The pair efficiency within STAR acceptance (single electron transverse momentum $p_{\mathrm{T}}^e > 0.2$ GeV/c, single electron pseudorapidity $|\eta_e| < 1$, dielectron rapidity $|y^{ee}| < 1$) is evaluated from the single electron efficiency by using a Monte Carlo (MC) simulation that used the virtual photons as the input and let them decay into dielectrons isotropically. The single-electron efficiency losses are caused by the detector inefficiency and electron identification cuts.

The detector efficiency includes the TPC tracking efficiency and TOF matching efficiency. The TPC tracking efficiency is evaluated via the standard STAR embedding technique [40]. The real data electrons from π^0 Dalitz decays and photon conversion are identified by invariant mass and used as the high purity electron sample to evaluate the TOF matching efficiency. Due to the limited statistics of this high purity electron sample, the pure pion sample selected by a tight $n\sigma_\pi$ cut is used to generate the three-dimensional (p_{T}, η, and ϕ) TOF matching efficiency. The p_{T}-dependent correction factor is then used to correct the TOF matching efficiency difference between electrons and pions caused by the decay loss of pions between the TPC and TOF, as well as other effects. The correction factor is the TOF matching efficiency ratio of electrons to pions as a function of p_{T}.

The electron identification efficiency includes two components: TOF $1/\beta$ cut efficiency and $n\sigma_e$ selection criteria efficiency. Both of these efficiencies are evaluated using the high purity electron samples identified by invariant mass.

The MC simulation, with virtual photons as input, is used to fold the single electron efficiency into the e^+e^- pair efficiency within STAR acceptance. The two-dimensional kinematics (M_{ee}, p_{T}) of the virtual photon is taken from the hadronic cocktail (discussed in Sec. III F). The virtual photons have flat rapidity and azimuthal distributions, and decay into e^+e^- pairs isotropically. The virtual photon simulation is also used to estimate the pair ϕ_V cut efficiency.

F. Hadronic cocktail

The detected e^+e^- pairs, originating from all stages in the evolution of heavy-ion collisions, are contributed by hadron decays (known as hadronic cocktail [42]) and photon-photon processes. The latter are mainly concentrated at low p_{T} [14]. The hadronic cocktail contributions in the final dielectron spectrum can be evaluated as long as the hadron yields dN/dy and p_{T} distributions are known. The hadronic cocktails included in our simulation contain contributions from decays of π^0, η, η', ω, ϕ, and J/ψ, as well as correlated charmed hadrons. The input rapidity distributions are assumed to be

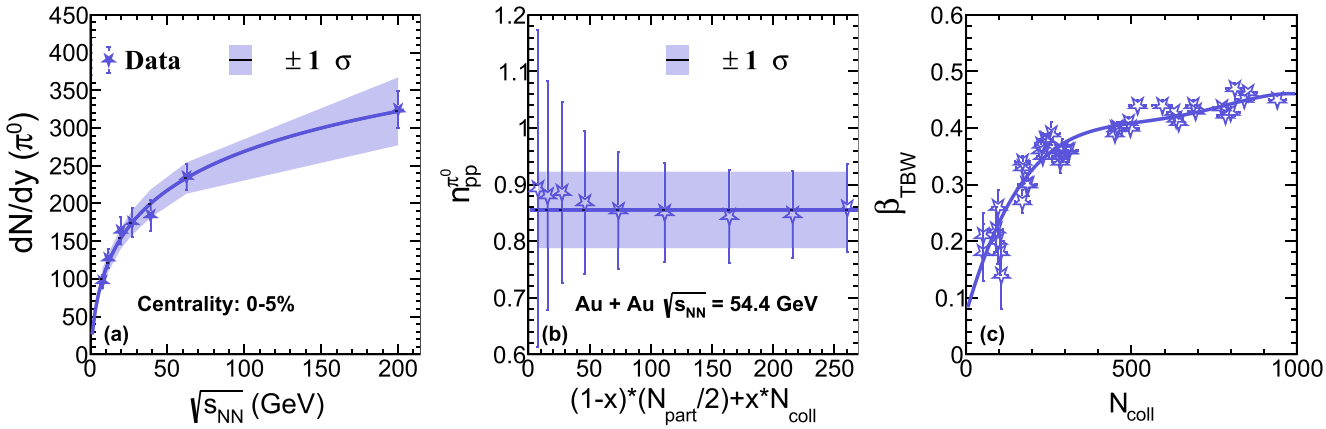

FIG. 4. (a) The π^0 yield [40,41] as a function of beam energy in 0–5% centrality with the exponential fit shown as the solid line. The band is the 1σ confidence interval of the fit. (b) The $n_{pp}^{\pi^0}$ value in different centralities at 54.4 GeV fitted by a constant shown as the solid line. The band is the 1σ confidence interval of the fit. (c) The parameter $\beta_{\rm TBW}$ for Tsallis blast wave fits as a function of $N_{\rm coll}$ with a polynomial fit shown as the solid line.

flat within $|y| < 1.2$. The input dN/dy and $p_{\rm T}$ distributions are discussed below.

The input π^0 yield is taken as the average of the π^+ and π^- yields. Other hadron yields are obtained by scaling by the ratio of the hadron to π^0 cross sections [43]. There were no measurements of hadron yields at 54.4 GeV, while the $\pi^\pm$ yields were accurately measured in the STAR BES-I program for 7.7, 11.5 19.6, 27, and 39 GeV [41] and in Ref. [40] for 62.4 and 200 GeV. The exponential function $p_0 \exp[-(x/p_1)^{p_2}]$ was used to fit the π^0 yields for these energies to interpolate the π^0 yields for the corresponding centrality at 54.4 GeV, where p_0, p_1, and p_2 are parameters. Figure 4(a) is an example of exponential fitting to interpolate the π^0 yield at 54.4 GeV in 0–5% centrality; the band is the 1σ confidence interval of the fit and was used as a systematic uncertainty in the cocktail. The "two components model" [44], given as

$$\frac{dN_{\pi^0}}{dy} = n_{pp}^{\pi^0}\left[(1-x)\frac{N_{\rm part}}{2} + xN_{\rm coll}\right], \tag{4}$$

is used to described the particles yield, where $N_{\rm coll}$ is the number of binary collisions and $N_{\rm part}$ is the number of participating nucleons. $N_{\rm coll}$ and $N_{\rm part}$ are obtained from the Glauber model [34] in our analysis. Therefore, according to the "two components model" [44], $n_{pp}^{\pi^0}$ in each centrality at 54.4 GeV can be obtained as shown in Fig. 4. At a given energy, $n_{pp}^{\pi^0}$ should be a constant, so fitting the data in Fig. 4(b) with a constant resulted in $n_{pp}^{\pi^0} = 0.855 \pm 0.068$ at 54.4 GeV. As before, the band is the 1σ confidence interval of the fit and was used as a systematic uncertainty in the cocktail. Based on Eq. (4), the yields of π^0 in the centralities 40–60%, 60–80%, and 80–100% at 54.4 GeV are 30.81 ± 2.44, 9.45 ± 0.75, and 2.74 ± 0.22, respectively. The charged pion yields for 200 GeV Au + Au minimum-bias collisions have been accurately measured in the STAR acceptance [40], so again the "two component model" was used to extrapolate the π^0 yield in 80–100% centrality at 200 GeV, where the π^0 yield was found to be 4.32 ± 0.31.

For light hadrons, the Tsallis blast-wave (TBW) functions provide good parametrizations of their $p_{\rm T}$ spectra [45]. Polynomial functions were used to fit the TBW parameters as a function of $N_{\rm coll}$ to extrapolate the parameters in our study. Figure 4(c) is an example of polynomial fitting to parameter $\beta_{\rm TBW}$ for the flow velocity in TBW. The extracted TBW parameters from the fit are used to generate the light hadron spectra as our input. The cocktail input of the J/ψ $p_{\rm T}$ spectra is the same as that in Ref. [46] at 62.4 GeV. We note that the hadronic cocktail for J/ψ are in a different mass range and phase space, though this should have little effect on our results.

The correlated open-charm decay contributions in $p+p$ collisions were obtained from PYTHIA simulations [47] and scaled by $N_{\rm coll}$ in Au + Au collisions for the default cocktail simulations. It should be noted that the Glauber model cannot describe experimental data due to trigger bias in peripheral collisions, so weights are included to correct charged particle multiplicities from the data to the Glauber model. In particular, the experimental data in 80–100% centrality have not been corrected for trigger bias, and therefore need to be studied. Figure 5(a) shows the dielectron yield as a function of centrality calculated by EPA-QED for the $\gamma\gamma \to e^+e^-$ process at 54.4 GeV [29]. Figure 5(b) is the multiplicity distribution of charged particles (N_{ch}) from our measurement compared to a Glauber model simulation at 54.4 GeV in 80–100% centrality. By taking the difference of the two distributions in Fig. 5(b), the effects of trigger bias on the dielectron yield from the $\gamma\gamma \to e^+e^-$ process at 54.4 GeV in 80–100% centrality can be determined. Thus, we conclude that the definition of 80–100% centrality at 54.4 GeV has a bias of 4.5% for the $\gamma\gamma \to e^+e^-$ process. Similarly, the definition of 80–100% centrality at 200 GeV has a bias of 1.3% for this process.

G. Systematic uncertainties

The sources of systematic uncertainty that contribute to the final result in this analysis includes: an efficiency correction, hadron contamination, and subtraction of the cocktail contri-

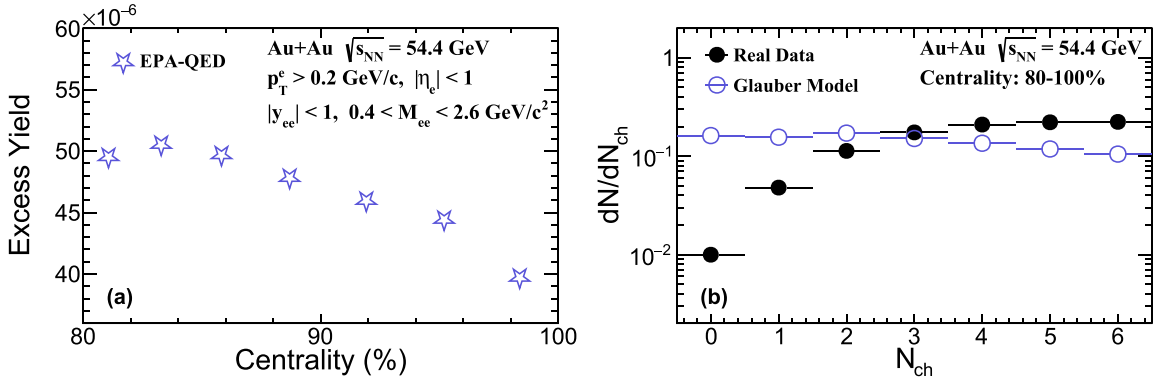

FIG. 5. (a) The dielectron yield of the $\gamma\gamma \to e^+e^-$ process as a function of centrality at 54.4 GeV calculated by EPA-QED. (b) The multiplicity distribution of charged particles (N_{ch}) at 54.4 GeV in 80–100% centrality for data and a Glauber model simulation.

bution. The systematic uncertainty on the efficiency correction comes from the uncertainty on the single-track reconstruction efficiency, which is estimated by comparing the embedding and data. A virtual photon simulation method was used to fold the uncertainty on the single-track efficiency to the pair systematic uncertainty. The pair systematic uncertainties for each individual component of the efficiency correction at $\sqrt{s_{NN}} = 54.4$ GeV are summarized in Table I. The systematic uncertainty of DCA is relatively large because the embedding does not describe the DCA distribution of the data well at 54.4 GeV. The systematic uncertainty on the efficiency correction at $\sqrt{s_{NN}} = 200$ GeV follows Ref. [37]. The electron candidates contain a small amount of hadron contamination, which may be combined with each other or electrons and thus contribute to the signal pairs. This contribution can be estimated by using the pure pion, kaon and proton samples, which results in an uncertainty of less than 2% at $\sqrt{s_{NN}} =$ 54.4 GeV as listed in Table I. The systematic uncertainty from hadron contamination is 5% at $\sqrt{s_{NN}} = 200$ GeV. The total systematic uncertainty of the signal is determined via the quadratic sum of the efficiency correction and hadron contamination. The systematic uncertainties on the cocktail are dominated by the extrapolated uncertainties on particle yields (discussed in Sec. III F) and the uncertainties on the decay branching ratios of hadrons to dielectrons as determined by the Particle Data Group [48]. Another important contribution is that of thermal radiation and ρ meson decays, which cannot be estimated by simulation. It is worth noting that the expected contribution from thermal radiation is also larger toward more central collisions. Given that hadrons freeze out at a particular temperature, and the average temperature from thermal radiation is similar, one expects therefore that the dielectrons from thermal radiation and ρ meson decays should have similar p_T distributions. In fact, in-medium ρ^0 decay dominates the low-p_T and low-mass dielectron range [46,49]. To take this into account, we scale the cocktail to match the data for $p_T \approx (0.2, 1.1)$ GeV/c and take this extra scaling factor as a systematic uncertainty in the cocktail. These contributions are included in the total systematic uncertainty of signal e^+e^- yield. The scale factors are determined to be 1.33, 1.06, and 1.47 at 40–60%, 60–80%, and 80-100% centralities at 54.4 GeV, respectively, and 1.23 in 80–100% centrality at 200 GeV.

TABLE I. Systematic uncertainties on pair efficiency and hadron contamination at 54.4 GeV.

	Source	Uncertainty (%)
TPC	nHitsFit	3.4
	nHitsdEdx	0.9
	DCA	9.1
	$n\sigma_e$	1.1
TOF	matching	0.1
	$1/\beta$	3.5
Hadron contamination		2
Total		10.7

IV. RESULTS AND DISCUSSION

A. Transverse momentum distributions

The p_T distributions of e^+e^- pairs within STAR acceptance ($p_T^e > 0.2$ GeV/c, $|\eta^e| < 1$, and $|y^{ee}| < 1$) for the invariant mass region 0.4–2.6 GeV/c^2 in Au + Au collisions at $\sqrt{s_{NN}} = 54.4$ and 200 GeV in different centralities are shown in Fig. 6. A significant enhancement in the yield is found below $p_T \approx 0.15$ GeV/c at these energies and centralities, while the hadronic cocktail, shown as the blue curve in Fig. 6, can describe the data reasonably well for $p_T > 0.15$ GeV/c. These excesses are consistent with the lowest order EPA-QED predictions for the collision of linearly polarized photons quantized from the extremely strong electromagnetic fields generated by the highly charged Au nuclei at ultrarelativistic speed [7]. We note that Fig. 6 panels (c) and (d) show that there may be potentially an enhanced yield at $p_T \simeq$ 0.2 GeV/c. We have examined single track and pair azimuthal and p_T distributions for those pairs to see if there is any correlation due to detector defects. We also checked pion contamination in the electron identification. None of these studies indicate that detector effects would cause such enhancement. Future high-statistic datasets with much smaller

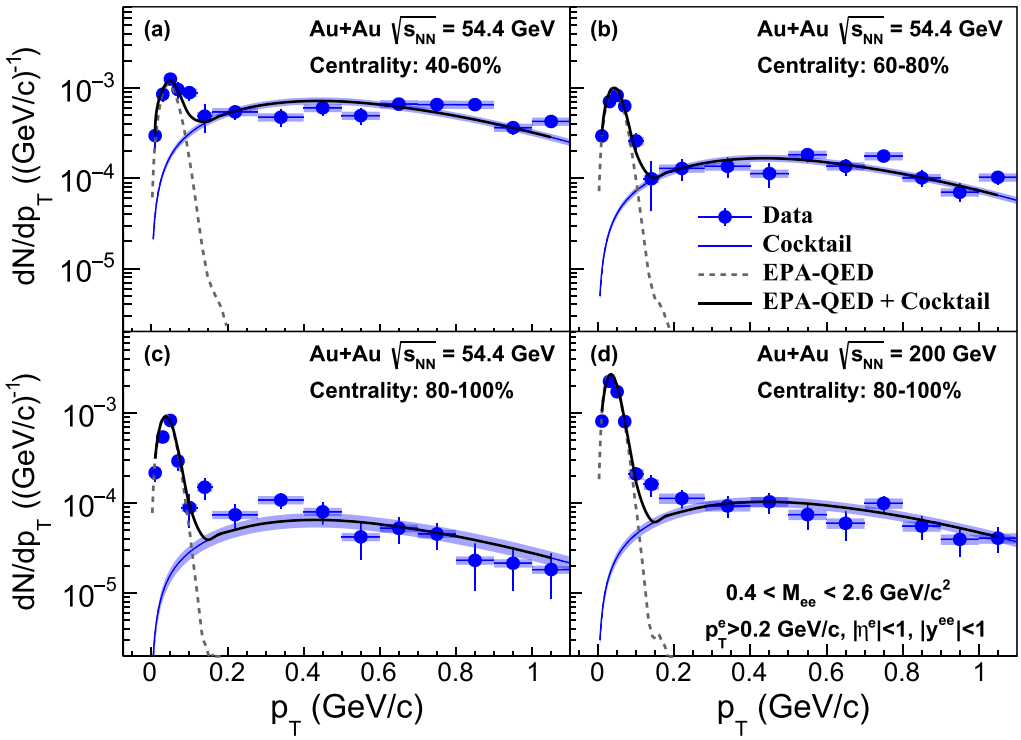

FIG. 6. The p_T distributions of e^+e^- pairs within the STAR acceptance for invariant mass region 0.4–2.6 GeV/c^2 in Au + Au collisions at $\sqrt{s_{NN}} = 54.4$ GeV in the centralities (a) 40–60%, (b) 60–80%, and (c) 80–100%, and (d) at $\sqrt{s_{NN}} = 200$ GeV for the 80–100% centrality range, compared to cocktail (solid blue line) and the lowest order EPA-QED predictions (dashed line) [29]. Statistical uncertainties are shown as vertical bars. The systematic uncertainties of the data are shown as blue boxes. The blue bands depict the systematic uncertainties of the cocktails.

trigger bias in peripheral Au + Au collisions at 200 GeV may help determine if this is a real physical effect.

B. Invariant mass distributions

After subtracting the hadronic cocktail contribution from the inclusive e^+e^- pairs, the invariant mass distributions of excess pairs for $p_T < 0.15$ GeV/c are shown in Fig. 7 for $\sqrt{s_{NN}} = 54.4$ and 200 GeV in different centralities. The invariant mass spectra are smooth and featureless even in the range of known vector mesons. This a consequence of the charge parity conservation allowing for J^{PC} states of two photons with positive C-parity only, irrespective of their virtuality. Thus, with the hadronic cocktail contributions removed, the remaining pairs are predominantly due to the photon-photon process of interest. These signal pairs are also consistent with the lowest order EPA-QED predictions [29].

We integrated the low-p_T invariant mass distributions for signal pairs in the invariant mass regions of (a) 0.4–0.76, (b) 0.76–1.2, and (c) 1.2–2.6 GeV/c^2. The integrated signal yields as a function of beam energy for the centrality intervals of 40–60%, 60–80%, and 80–100% are shown in Fig. 8. We note that the signal yields in a given centrality increase with beam energy in all three mass regions. EPA-QED [29] predicts similar energy dependences, which are consistent with the data.

C. p_T^2 distributions

To further explore the properties of dielectrons produced via the Breit-Wheeler process, the p_T^2 distributions of the signal pairs within STAR acceptance in the invariant mass region of 0.4–0.76 GeV/c^2 in different centralities at 54.4 and 200 GeV are shown in Fig. 9. The aforementioned lowest order numerical EPA-QED calculations are also shown in the plots as dotted lines, which are consistent with the data within uncertainties.

Since $\sqrt{\langle p_T^2 \rangle}$ is more sensitive to p_T broadening than the distribution of p_T itself, we study $\sqrt{\langle p_T^2 \rangle}$ for e^+e^- pairs as a function of beam energy in the invariant mass region of 0.4–0.76 GeV/c^2 in different centralities, as shown in Fig. 10. Due to statistical limitations, EPA-QED results are used to extrapolate to the unmeasured higher p_T^2 region to account for the missing contribution. One can see that $\sqrt{\langle p_T^2 \rangle}$ decreases with increasing impact parameter at both beam energies. This results from the impact parameter dependence of the transverse momentum of the initial photon. For high precision results at $\sqrt{s_{NN}} = 200$ GeV in UPCs, the consistency between the EPA-QED prediction [29] and our measurement shows that the EPA-QED predictions at $\sqrt{s_{NN}} = 200$ GeV can be treated as a baseline. A difference of 4.3σ is found when comparing the data at $\sqrt{s_{NN}} = 54.4$ GeV to EPA-QED predictions at $\sqrt{s_{NN}} = 200$ GeV, which arises from the energy

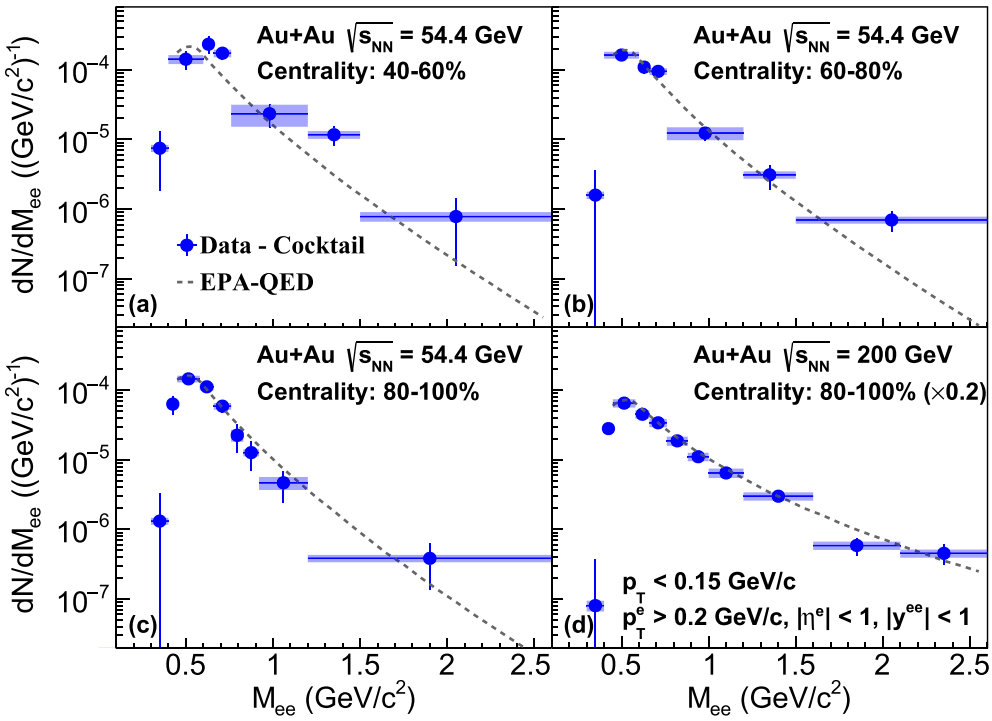

FIG. 7. The low-p_T ($p_T < 0.15$ GeV/c) e^+e^- excess mass spectra (data − cocktail) within the STAR acceptance in Au + Au collisions at $\sqrt{s_{NN}} = 54.4$ GeV in the centralities (a) 40–60%, (b) 60–80%, and (c) 80–100%, and (d) at $\sqrt{s_{NN}} = 200$ GeV for the 80–100% centrality range (scaled × 0.2), compared to the lowest order EPA-QED predictions (dashed line) [29]. Statistical uncertainties are shown as vertical bars, while systematic uncertainties are shown as blue boxes.

dependence of $\sqrt{\langle p_T^2 \rangle}$ and possible final-state effects. The observed energy dependence shows that $\sqrt{\langle p_T^2 \rangle}$ decreases with increasing beam energy, which is consistent with EPA-QED predictions. Final-state effects will be discussed in Sec. IV E.

D. $\Delta\phi$ distributions

A consequence of the quantum nature of the real photon intrinsic spin and wave function is that the parallel and perpendicular relative polarization angles in photon-photon collisions result in distinct differential cross sections [28,51]. It was only recently realized that these effects could be accessed experimentally in ultrarelativistic heavy-ion collisions [52] since the transverse momentum of the pair is correlated with the polarization of the photons. For linearly polarized photons, the distinct differential cross sections contains noticeable $\cos(4\Delta\phi)$ and negligible $\cos(2\Delta\phi)$ terms, where $\Delta\phi$ is the azimuthal angle difference between the momenta of the

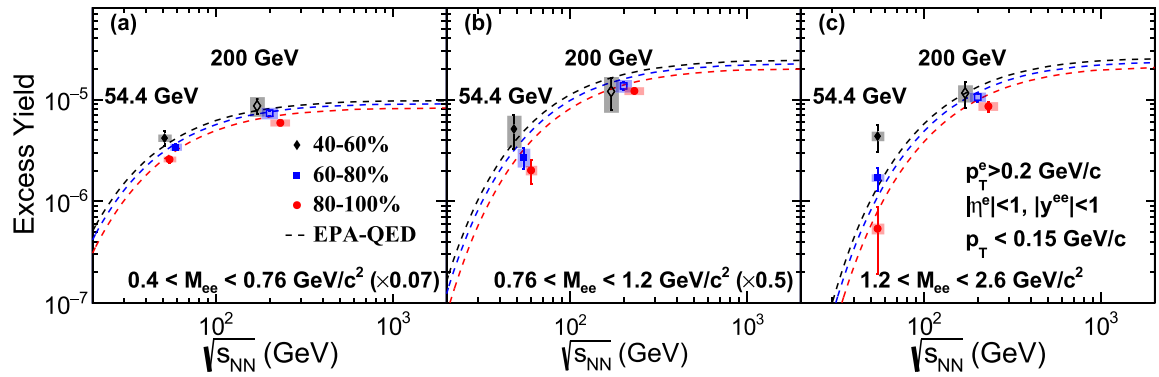

FIG. 8. The integrated signal e^+e^- yields as a function of collision energy in the mass regions of (a) 0.4–0.76 GeV/c^2 (scaled × 0.07), (b) 0.76–1.2 GeV/c^2 (scaled × 0.5), and (c) 1.2–2.6 GeV/c^2 in Au + Au collisions in the 40–60%, 60–80%, and 80–100% centrality ranges. The points are offset slightly in the horizontal direction for clarity. The energy dependence of integrated signal e^+e^- yields from the lowest order EPA-QED predictions [29] are also shown as dashed lines for comparison. Statistical uncertainties are shown as vertical bars. The systematic uncertainties of the data are shown as boxes. Open markers are extracted from previously published STAR data in Ref. [14].

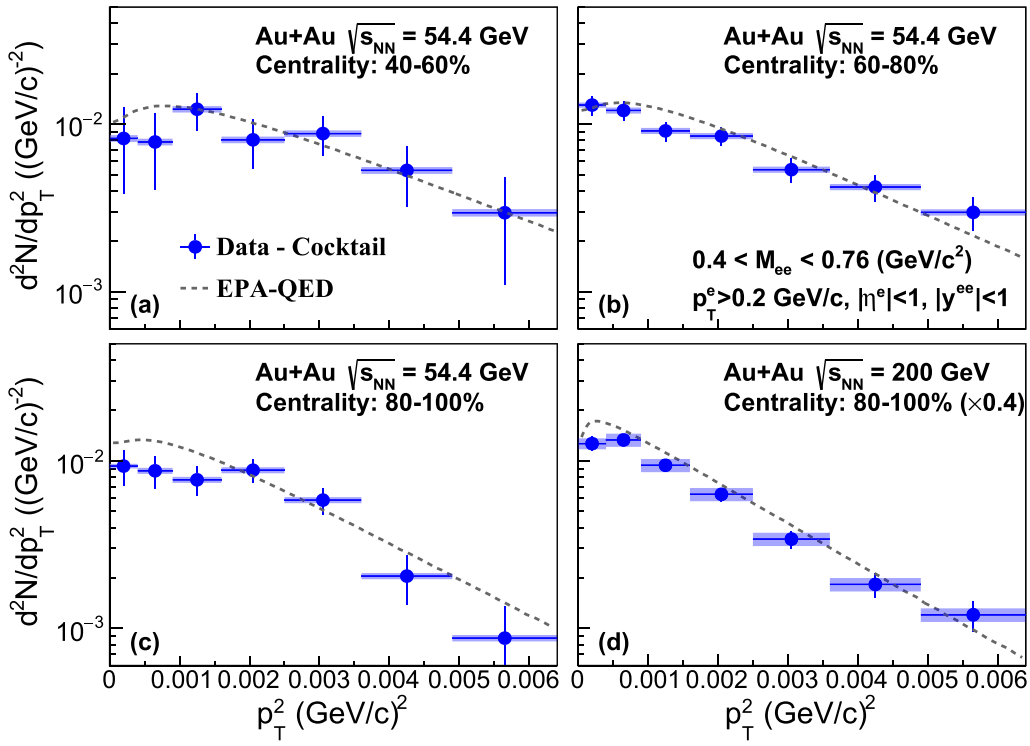

FIG. 9. The p_T^2 distributions of the signal dielectrons within STAR acceptance in the mass region of 0.4–0.76 GeV/c^2 at $\sqrt{s_{NN}}$ = 54.4 GeV in the centralities (a) 40–60%, (b) 60–80%, and (c) 80–100%, and (d) at $\sqrt{s_{NN}}$ = 200 GeV for the 80–100% centrality range (scaled × 0.4), compared to the lowest order EPA-QED predictions (dashed line) [29]. Statistical uncertainties are shown as vertical bars. The systematic uncertainties are shown as blue boxes.

e^+e^- and $\vec{p_{e^+}} - \vec{p_{e^-}}$ (or $\vec{p_{e^-}} - \vec{p_{e^+}}$), in the laboratory frame. Since the photoinduced e^+e^- pairs are produced almost back to back, the $\Delta\phi$ is approximately the azimuthal angle in the laboratory frame between the momentum of the e^+e^- pair and one of the daughters (e^+ or e^-). Recently, STAR observed cos(4$\Delta\phi$) modulations in peripheral and ultraperipheral Au + Au collisions at 200 GeV, and declared that it is closely related to the phenomenon of vacuum birefringence [19].

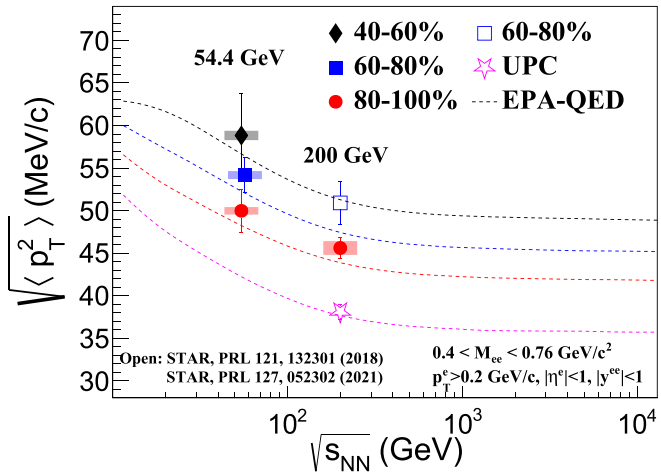

FIG. 10. The $\sqrt{\langle p_T^2 \rangle}$ of e^+e^- pairs as a function of beam energy compared to the lowest order EPA-QED predictions [29] shown as dashed lines in Au + Au collisions for the centrality intervals of 40–60%, 60–80%, 80–100% and for UPCs. The pair invariant mass region is 0.4–0.76 GeV/c^2. The solid blue marker is offset slightly in the horizontal direction for clarity. Statistical uncertainties are shown as vertical bars, while systematic uncertainties are shown as boxes. Open markers are extracted from previously published STAR data in Refs. [14,19].

Figure 11 shows the $\Delta\phi$ distribution within STAR acceptance for invariant mass region 0.45–0.76 GeV/c^2 in Au + Au collisions at $\sqrt{s_{NN}}$ = 54.4 and 200 GeV in different centralities. The fits to a function of the form given as

$$f(\Delta\phi) = C[1 - A_{4\Delta\phi}\cos(4\Delta\phi)] \quad (5)$$

are also shown in Fig. 11 as solid lines. In Eq. (5), C is a constant, and $A_{4\Delta\phi}$ is the magnitude of cos(4$\Delta\phi$) modulation. The observed magnitudes of the cos(4$\Delta\phi$) modulations are presented in Table II; the first and second uncertainties are statistical and systematic uncertainties, respectively. The χ^2/NDF for the fit of Eq. (5) is also shown in Table II. In 60–80% centrality at 54.4 GeV and 80–100% centrality at 200 GeV, there are statistically significant indications of nonzero cos(4$\Delta\phi$) modulation. At 54.4 GeV, due to a large background from the hadronic cocktail in 40–60% centrality and limited statistics of photon-produced dielectrons in 80–100% centrality, cos(4$\Delta\phi$) modulations are consistent with 0 within uncertainties. Our results are also compared with the lowest order EPA-QED predictions for the collision of linearly polarized photons, shown in Fig. 11 as a dashed line. The extracted ($A_{4\Delta\phi}$) and χ^2/NDF values of cos(4$\Delta\phi$) are shown in Table II.

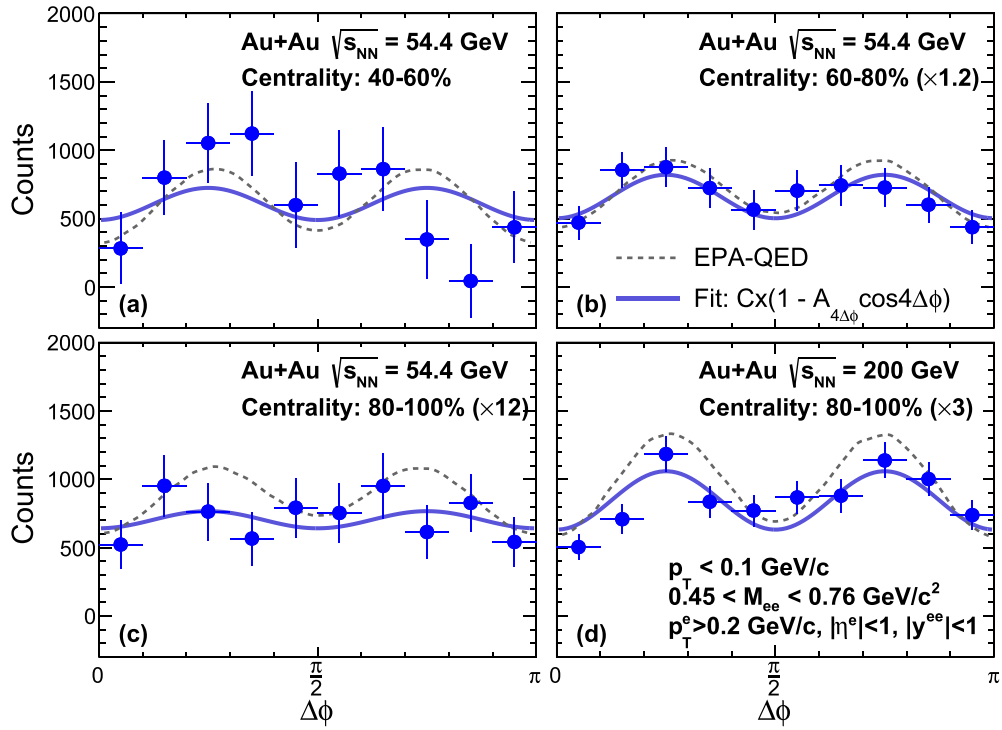

FIG. 11. The $\Delta\phi$ distributions of signal dielectrons in Au + Au collisions at $\sqrt{s_{NN}} = 54.4$ GeV in the centralities (a) 40–60%, (b) 60–80% (scaled × 1.2), and (c) 80–100% (scaled × 12), and at (d) $\sqrt{s_{NN}} = 200$ GeV for the 80–100% centrality range (scaled × 3). The pair invariant mass region is 0.45–0.76 GeV/c^2 and pair $p_T < 0.1$ GeV/c. Statistical uncertainties are shown as vertical bars. The full curves are the results of the fits according to Eq. (5) (solid curves) compared with EPA-QED predictions (dashed curves) [29].

The amplitude of $\cos(4\Delta\phi)$, or $(A_{4\Delta\phi})$, is shown as a function of p_T in Fig. 12(a) for 80–100% centrality and in Fig. 12(b) for UPCs at 200 GeV. For UPC events, there is no hadronic or medium-induced background in the selected kinematic range. For more details on the selection and analysis of these events, see Ref. [19]. It can be seen that the $\cos(4\Delta\phi)$ modulation has obvious p_T dependence in UPCs. More specifically, below $p_T \approx 0.08$ GeV/c the $\cos(4\Delta\phi)$ modulation amplitude remains positive, then turns increasingly negative for p_T above 0.08 GeV/c in UPCs. However, no obvious p_T dependence is observed in 80–100% centrality due to the limited statistics. The figure shows two types of QED calculations [53]. They are the lowest order QED shown as the black dashed line, and QED with higher order effects due to perturbative final state soft photon radiation (Sudakov effect) shown as the red dashed line. The difference between the two QED calculations is small for p_T less than about 0.08 GeV/c, and STAR statistical precision is not sufficient to distinguish between them so far. At higher p_T, however, UPC measurements are consistent with QED when the Sudakov effects are included. Our measurements show the importance of including the radiation of final-state soft photons in UPCs.

E. Application: Constrain the Au nuclear charge distribution

The photon density is related to the energy flux of the electromagnetic fields [8] $n(\omega) \propto \vec{S} = \frac{1}{\mu_0}\vec{E} \times \vec{B}$, where μ_0 is vacuum permeability, and $\vec{S}$ is the Poynting vector. Total and differential cross sections for $\gamma\gamma \to e^+e^-$ are related to field strength and spatial distribution. Therefore, assuming the electromagnetic field comes from the charged nucleus, it was proposed that the cross section of $\gamma\gamma \to e^+e^-$ can be used to constrain the nuclear charge distribution [18,29]. Figure 13 shows the 99.7% (3σ) confidence level contours for the charge distribution of Au nucleus with different data conditions. These confidence contours result from a χ^2-minimization

TABLE II. The amplitudes ($A_{4\Delta\phi}$) of $\cos(4\Delta\phi)$ and χ^2/NDF of the fits according to Eq. (5), compared with EPA-QED predictions.

	Fit		EPA-QED	
	$A_{4\Delta\phi}$	χ^2/NDF	$A_{4\Delta\phi}$	χ^2/NDF
54.4 GeV 40–60%	$0.19 \pm 0.21 \pm 0.03$	13.24/8	0.40	12.40/9
54.4 GeV 60–80%	$0.24 \pm 0.09 \pm 0.04$	4.82/8	0.31	4.94/9
54.4 GeV 80–100%	$0.09 \pm 0.13 \pm 0.01$	4.98/8	0.24	13.04/9
200 GeV 80–100%	$0.25 \pm 0.06 \pm 0.03$	12.95/8	0.35	26.97/9

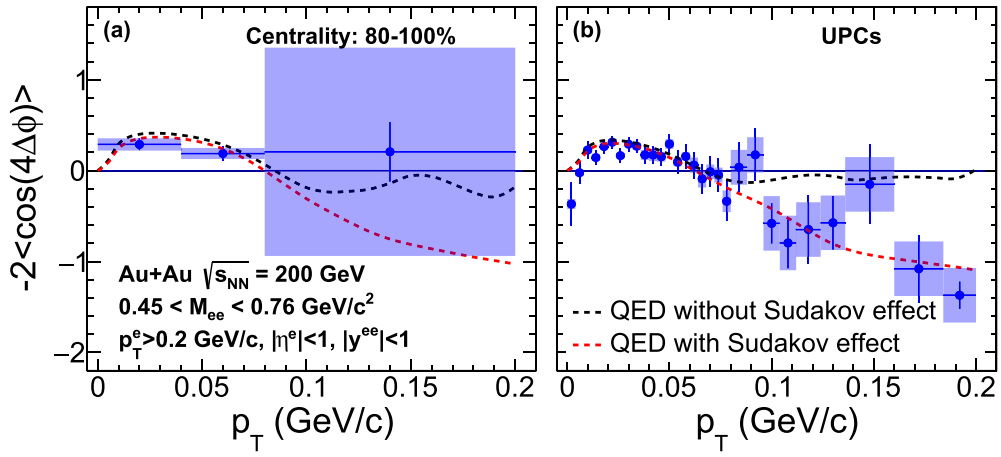

FIG. 12. The amplitude of $\cos(4\Delta\phi)$, $A_{4\Delta\phi}$, in (a) 80–100% centrality and (b) UPCs at 200 GeV compared to the different EPA-QED predictions [50]. The pair invariant mass region is 0.45–0.76 GeV/c^2. The black line shows the lowest order QED calculation, while the red line shows the QED calculation with high order effect (Sudakov effect). Statistical uncertainties are shown as vertical bars, while systematic uncertainties are shown as blue boxes.

procedure applied to the previous STAR measurements [14,19] and these new measurements of the p_T and M_{ee} distributions from the $\gamma\gamma \to e^+e^-$ process compared to the corresponding lowest order EPA-QED calculations. For the minimization, the nuclear radius and skin depth are parametrized according to the Woods-Saxon distribution and are assumed to be the same for both electromagnetic and strong interactions. The Woods-Saxon distribution is given by

$$\rho_A(r) = \frac{\rho_0}{1 + \exp[(r - R)/d]}, \tag{6}$$

where R is the nuclear radius and d is the skin depth. The absolute cross section is used to obtain the χ^2 value. The data points in peripheral Au + Au collisions at 54.4 and 200 GeV were used to obtain the blue and green contours, respectively. All available data points in Au + Au peripheral collisions at both 200 GeV [14] and 54.4 GeV were used to obtain the red contour. The data points in ultraperipheral Au + Au collisions at 200 GeV [19] were used to get the gray contour. In order to incorporate the experimental conditions into the theoretical calculations, the QED calculation in UPCs has included the probability of emitting neutrons from an excited nucleus $1n1n$, where $1n1n$ is defined as two colliding nuclei that each emit a neutron.

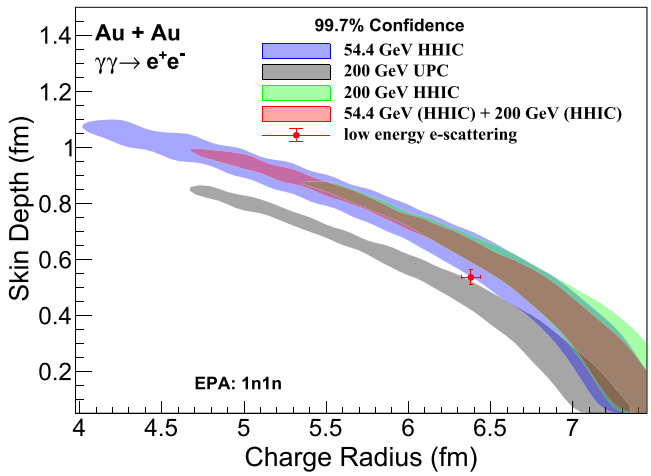

FIG. 13. The constraints on Au nuclear charge distribution extracted by the comparison between STAR measurement of $\gamma\gamma \to e^+e^-$ and the corresponding lowest order EPA-QED calculation [29]. HHICs include 40–60%, 60–80%, and 80–100% centralities.

The red marker shown in Fig. 13 indicates the result from fits to low energy electron scattering data [54]. The gray contour deviates from blue, green, and red contours but is quite close to the red marker, which indicates a potential final-state effect in peripheral hadronic heavy-ion collisions that is not included in the EPA-QED calculations. e^+e^- pairs produced from photon-photon interactions are mostly back to back, and final-state effects due to trapped magnetic field or Coulomb scattering in the QGP can lead to the observed p_T broadening. As Fig. 10 shows, all non-UPC data points are slightly higher than QED predictions at about the 2.19σ confidence level. For different radius and skin depth, we can get different root-mean-square (rms) values of the radius according to Eq. (6). Then according to the minimum χ^2 ($\chi^2_{\rm min}$) and the corresponding uncertainty we can get the rms charge radius corresponding to the different conditions in Fig. 13, which are listed in Table III. These are compared to the default rms value of the nuclear charge radius of $\sqrt{\langle r^2 \rangle} = 5.33$ fm at

TABLE III. The rms radius ($\sqrt{\langle r^2 \rangle}$) at minimum χ^2 ($\chi^2_{\rm min}$) and uncertainties within $\chi^2_{\rm min} + 1$.

	rms charge radius (fm)
Low energy e-scattering experiment	5.33 ± 0.05
200 GeV (UPC)	5.39 + 0.16 - 0.21
54.4 GeV (HHIC)	5.39 + 0.16 - 0.30
200 GeV (HHIC)	5.72 + 0.07 - 0.04
54.4 GeV (HHIC) + 200 GeV (HHIC)	5.72 + 0.03 - 0.14

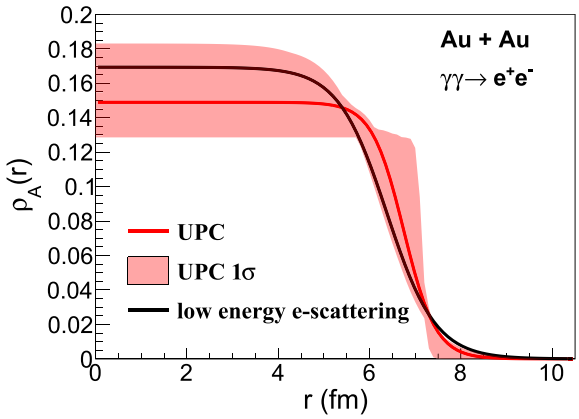

FIG. 14. The density of nucleons inside a Au nuclear, which is parameterized with a Woods-Saxon form. The black solid line represents the results from low energy *e*-scattering experiment, while the red solid line shows the minimum χ^2 result for the 200 GeV UPC fit. The red contour corresponds to the 1σ ($\chi^2_{\rm min}+1$) confidence interval in the UPC.

$R = 6.38$ fm and $d = 0.535$ fm [54]. The rms nuclear charge radius extracted by data points at 200 GeV for ultraperipheral collisions is consistent with the default value, while the result extracted from hadronic heavy-ion collisions at 200 GeV is slightly larger (by about 0.4 fm) than the default value. Although the rms nuclear charge radius at 54.4 GeV HHIC is consistent with the value from low energy electron scattering, the uncertainty is large, and when the 54.4 and 200 GeV HHICs are combined, the large rms value is still favored. These all indicate that a potential final-state effect in hadronic heavy-ion collisions can modify the results of the charge radius extraction and favors an apparent large radius. Finally, we present the density of nucleons inside a gold nucleus extracted from UPC data, as indicated by the red solid line in the Fig. 14, which is parametrized with a Woods-Saxon form. The red band represents the 1σ ($\chi^2_{\rm min}+1$) confidence interval in the UPCs. For comparison, the black solid line in the Fig. 14 represents the results from low energy electron scattering experiments. It can be seen that within the 1sigma uncertainty, the UPC results are consistent with the black solid line.

V. CONCLUSIONS

We have reported low-$p_{\rm T}$ dielectron measurements in peripheral Au + Au collisions at $\sqrt{s_{NN}} = 54.4$ and 200 GeV by the STAR experiment at RHIC. The measured dielectron transverse momentum spectrum shows a significant excess at low $p_{\rm T}$ ($p_{\rm T} < 0.15$ GeV/c) with respect to expected hadronic contributions at both beam energies. The extracted excess yield at low $p_{\rm T}$ as a function of dielectron invariant mass shows a smooth and featureless distribution, which is a consequence of the quantum numbers of the two photons involved in the Breit-Wheeler process. The integrated signal e^+e^- yields in the dielectron invariant mass regions of 0.4–0.76, 0.76–1.2, and 1.2–2.6 GeV/c^2 show significant energy dependence in different centralities, and the results are consistent with the EPA-QED predictions. $\sqrt{\langle p_{\rm T}^2\rangle}$ decreases with increasing impact parameter at both beam energies, while its distribution strongly suggests both an energy dependence and that final-state effects may play a role. The $\Delta\phi$ distribution shows $\cos(4\Delta\phi)$ modulations at $p_{\rm T} < 0.1$ GeV/c with 2.4σ and 3.7σ significance at 54.4 GeV in 60–80% centrality and 200 GeV in 80–100% centrality, respectively. Due to statistical limitations, the $\cos(4\Delta\phi)$ modulations in other centralities and energies are consistent with 0 within uncertainties. However, $\cos(2\Delta\phi)$ modulations are found to be consistent with 0 within uncertainty for $p_{\rm T} < 0.1$ GeV/c in all centralities at both beam energies. $-2\langle\cos(4\Delta\phi)\rangle$ shows a clear $p_{\rm T}$ dependence in ultraperipheral collisions. In the high $p_{\rm T}$ region ($p_{\rm T} > 0.1$ GeV/c), the behavior of $-2\langle\cos(4\Delta\phi)\rangle$ as a function of $p_{\rm T}$ indicates that the Sudakov effects need to be included in theoretical calculations. However, this effect does not lead to qualitative conclusions in 80–100% centrality due to statistical limitations. Finally, we confirmed that measurements of the $\gamma\gamma \to e^+e^-$ process can be used to constrain nuclear charge distributions at RHIC energies, though a potential final-state effect in hadronic heavy-ion collisions can modify the extracted nuclear charge radius in a way that favors a larger radius.

ACKNOWLEDGMENTS

We thank the RHIC Operations Group and SDCC at BNL, the NERSC Center at LBNL, and the Open Science Grid consortium for providing resources and support. This work was supported in part by the Office of Nuclear Physics within the U.S. DOE Office of Science, the U.S. National Science Foundation, National Natural Science Foundation of China, Chinese Academy of Science, the Ministry of Science and Technology of China and the Chinese Ministry of Education, NSTC Taipei, the National Research Foundation of Korea, Czech Science Foundation and Ministry of Education, Youth and Sports of the Czech Republic, Hungarian National Research, Development and Innovation Office, New National Excellency Programme of the Hungarian Ministry of Human Capacities, Department of Atomic Energy and Department of Science and Technology of the Government of India, the National Science Centre and WUT ID-UB of Poland, the Ministry of Science, Education and Sports of the Republic of Croatia, German Bundesministerium für Bildung, Wissenschaft, Forschung and Technologie (BMBF), Helmholtz Association, Ministry of Education, Culture, Sports, Science, and Technology (MEXT), Japan Society for the Promotion of Science (JSPS) and Agencia Nacional de Investigación y Desarrollo (ANID) of Chile.

[1] C. F. von Weizsacker, Radiation emitted in collisions of very fast electrons, Z. Phys. **88**, 612 (1934).

[2] E. J. Williams, Nature of the high-energy particles of penetrating radiation and status of ionization and radiation formulae, Phys. Rev. **45**, 729 (1934).

[3] G. Baur *et al.*, Coherent $\gamma\gamma$ and γA interactions in very peripheral collisions at relativistic ion colliders, Phys. Rep. **364**, 359 (2002).

[4] C. A. Bertulani *et al.*, Physics of ultra-peripheral nuclear collisions, Annu. Rev. Nucl. Part. Sci. **55**, 271 (2005).

[5] A. J. Baltz, The physics of ultraperipheral collisions at the LHC, Phys. Rep. **458**, 1 (2008).

[6] S. Klein and P. Steinberg, Photonuclear and two-photon interactions at high-energy nuclear colliders, Annu. Rev. Nucl. Part. Sci. **70**, 323 (2020).

[7] W. Zha *et al.*, Initial transverse-momentum broadening of Breit-Wheeler process in relativistic heavy-ion collisions, Phys. Lett. B **800**, 135089 (2020).

[8] M. Vidovic, M. Greiner, C. Best, and G. Soff, Impact parameter dependence of the electromagnetic particle production in ultrarelativistic heavy ion collisions, Phys. Rev. C **47**, 2308 (1993).

[9] J. Adams *et al.* (STAR Collaboration), Production of e^+e^- pairs accompanied by nuclear dissociation in ultraperipheral heavy ion collisions, Phys. Rev. C **70**, 031902(R) (2004).

[10] E. Abbas *et al.* (ALICE Collaboration), Charmonium and e^+e^- pair photoproduction at mid-rapidity in ultra-peripheral Pb-Pb collisions at $\sqrt{s_{\rm NN}} = 2.76$ TeV, Eur. Phys. J. C **73**, 2617 (2013).

[11] S. R. Klein *et al.*, STARlight: A Monte Carlo simulation program for ultra-peripheral collisions of relativistic ions, Comput. Phys. Commun. **212**, 258 (2017).

[12] A. J. Baltz, Y. Gorbunov, S.R. Klein, and J. Nystrand, Two-photon interactions with nuclear breakup in relativistic heavy ion collisions, Phys. Rev. C **80**, 044902 (2009).

[13] K. Hencken *et al.*, Photon-photon luminosities in relativistic heavy ion collisions at LHC energies, Z. Phys. C **68**, 473 (1995).

[14] J. Adam *et al.* (STAR Collaboration), Low-$p_T e^+e^-$ pair production in Au + Au collisions at $\sqrt{s_{NN}} = 200$ GeV and U + U collisions at $\sqrt{s_{NN}} = 193$ GeV at STAR, Phys. Rev. Lett. **121**, 132301 (2018).

[15] M. Aaboud *et al.* (ATLAS Collaboration), Observation of centrality-dependent acoplanarity for muon pairs produced via two-photon scattering in Pb+Pb collisions at $\sqrt{s_{NN}} = 5.02$ TeV with the ATLAS detector, Phys. Rev. Lett. **121**, 212301 (2018).

[16] E. Abbas *et al.* (ALICE Collaboration), Dielectron production at low transverse momentum in Pb-Pb collisions at $\sqrt{s_{\rm NN}} = 5.02$ TeV with ALICE, PoS **LHCP2019**, 164 (2019).

[17] A. M. Sirunyan *et al.* (CMS Collaboration), Observation of forward neutron multiplicity dependence of dimuon acoplanarity in ultraperipheral Pb-Pb collisions at $\sqrt{s_{NN}} = 5.02$ TeV, Phys. Rev. Lett. **127**, 122001 (2021).

[18] J. D. Brandenburg *et al.*, Mapping the electromagnetic fields of heavy-ion collisions with the Breit-Wheeler process, Eur. Phys. J. A **57**, 299 (2021).

[19] J. Adam *et al.* (STAR Collaboration), Measurement of e^+e^- momentum and angular distributions from linearly polarized photon collisions, Phys. Rev. Lett. **127**, 052302 (2021).

[20] M. Kłusek-Gawenda *et al.*, Centrality dependence of dilepton production via $\gamma\gamma$ processes from Wigner distributions of photons in nuclei, Phys. Lett. B **814**, 136114 (2021).

[21] S. Lin, R.-J. Wang, J.-F. Wang, H.-J. Xu, S. Pu, and Q. Wang, Photoproduction of e^+e^- in peripheral isobar collisions, Phys. Rev. D **107**, 054004 (2023).

[22] L. D. Landau and E. M. Lifschitz, On the production of electrons and positrons by a collision of two particles, Phys. Z. Sowjetunion **6**, 244 (1934).

[23] H. Bethe and W. Heitler, On the stopping of fast particles and on the creation of positive electrons, Proc. R. Soc. London A **146**, 83 (1934).

[24] G. Breit and J. A. Wheeler, Collision of two light quanta, Phys. Rev. **46**, 1087 (1934).

[25] S. Klein, A. H. Mueller, B. W. Xiao, and F. Yuan, Lepton pair production through two photon process in heavy ion collisions, Phys. Rev. D **102**, 094013 (2020).

[26] L. Esnault *et al.*, Electron-positron pair production in the collision of real photon beams with wide energy distributions, Plasma Phys. Control. Fusion **63**, 125015 (2021).

[27] Q. Zhao *et al.*, Signatures of linear Breit-Wheeler pair production in polarized $\gamma\gamma$ collisions, Phys. Rev. D **105**, L071902 (2022).

[28] V. M. Budnev *et al.*, The two photon particle production mechanism. Physical problems. Applications. Equivalent photon approximation, Phys. Rep. **15**, 181 (1975).

[29] X. Wang, J.D. Brandenburg, L. Ruan, F. Shao, Z. Xu, C. Yang, and W. Zha, Collision-energy dependence of the Breit-Wheeler process in heavy-ion collisions and its application to nuclear charge radius measurements, Phys. Rev. C **107**, 044906 (2023).

[30] I. Alekseev *et al.*, Polarized proton collider at RHIC, Nucl. Instrum. Methods Phys. Res., Sect. A **499**, 392 (2003).

[31] M. Anderson *et al.*, The STAR time projection chamber: a unique tool for studying high multiplicity events at RHIC, Nucl. Instrum. Methods Phys. Res., Sect. A **499**, 659 (2003).

[32] P. Fachini *et al.*, Propoal for a large area time of flight system for STAR, STAR Technical Note No. SN0621, Nucl. Instrum. Meth. A 508, 181 (2003).

[33] W. J. Llope *et al.*, The STAR vertex position detector, Nucl. Instrum. Methods Phys. Res., Sect. A **759**, 23 (2014).

[34] M. L. Miller *et al.*, Glauber modeling in high energy nuclear collisions, Annu. Rev. Nucl. Part. Sci. **57**, 205 (2007).

[35] M. Abdallah *et al.* (STAR Collaboration), Azimuthal anisotropy measurement of (multi)strange hadrons in Au+Au collisions at $\sqrt{s_{NN}} = 54.4$ GeV, Phys. Rev. C **107**, 024912 (2023).

[36] M. Shao *et al.*, Extensive particle identification with TPC and TOF at the STAR experiment, Nucl. Instrum. Methods Phys. Res., Sect. A **558**, 419 (2006).

[37] L. Adamczyk *et al.* (STAR Collaboration), Measurements of dielectron production in Au + Au collisions at $\sqrt{s_{NN}} = 200$ GeV from the STAR experiment, Phys. Rev. C **92**, 024912 (2015).

[38] A. Adare *et al.* (PHENIX Collaboration), Detailed measurement of the e^+e^- pair continuum in $p + p$ and Au+Au collisions at $\sqrt{s_{NN}} = 200$ GeV and implications for direct photon production, Phys. Rev. C **81**, 034911 (2010).

[39] L. Adamczyk *et al.* (STAR Collaboration), Dielectron mass spectra from Au+Au collisions at $\sqrt{s_{NN}} = 200$ GeV, Phys. Rev. Lett. **113**, 022301 (2014).

[40] B. I. Abelev *et al.* (STAR Collaboration), Systematic measurements of identified particle spectra in $p + p$, $d +$ Au, and Au+Au collisions from STAR, Phys. Rev. C **79**, 034909 (2009).

[41] L. Adamczyk *et al.* (STAR Collaboration), Bulk properties of the medium produced in relativistic heavy-ion collisions

from the beam energy scan program, Phys. Rev. C **96**, 044904 (2017).
[42] J. Chen *et al.*, Properties of the QCD matter – An experimental review of selected results from RHIC BES program, Nucl. Sci. Tech. **35**, 214 (2024).
[43] G. Agakichiev *et al.* (CERES Collaboration), e^+e^--pair production in Pb-Au collisions at 158 GeV per nucleon, Eur. Phys. J. C **41**, 475 (2005).
[44] D. Kharzeev and M. Nardi, Hadron production in nuclear collisions at RHIC and high density QCD, Phys. Lett. B **507**, 121 (2001).
[45] J. Chen, J. Deng, Z. Tang, Z. Xu, and L. Yi, Nonequilibrium kinetic freeze-out properties in relativistic heavy ion collisions from energies employed at the RHIC beam energy scan to those available at the LHC, Phys. Rev. C **104**, 034901 (2021).
[46] J. Adam *et al.* (STAR Collaboration), Measurements of dielectron production in Au + Au collisions at $\sqrt{s_{NN}} = 27$, 39, and 62.4 GeV from the STAR experiment, Phys. Rev. C **107**, L061901 (2023).
[47] T. Sjostrand *et al.*, High-energy physics event generation with PYTHIA 6.1, Comput. Phys. Commun. **135**, 238 (2001).
[48] P. A. Zyla *et al.* (Particle Data Group), Review of particle physics, Prog. Theor. Exp. Phys. **2020**, 083C01.
[49] R. Rapp and H. van Hees, Thermal electromagnetic radiation in heavy-ion collisions, Eur. Phys. J. A **52**, 257 (2016).
[50] D. Y. Shao, C. Zhang, J. Zhou, and Y. J. Zhou, Azimuthal asymmetries of muon pair production in ultraperipheral heavy ion collisions, Phys. Rev. D **107**, 036020 (2023).
[51] L. A. Harland-Lang *et al.*, Exclusive LHC physics with heavy ions: SuperChic 3, Eur. Phys. J. C **79**, 39 (2019).
[52] C. Li *et al.*, Probing the linear polarization of photons in ultraperipheral heavy ion collisions, Phys. Lett. B **795**, 576 (2019).
[53] D. Y. Shao, C. Zhang, J. Zhou, and Y. J. Zhou, Lepton pair production in ultraperipheral collisions: Toward a precision test of the resummation formalism, Phys. Rev. D **108**, 116015 (2023).
[54] H. De Vries *et al.*, Nuclear charge-density-distribution parameters from elastic electron scattering, At. Data Nucl. Data Tables **36**, 495 (1987).